

Optical Engineering

SPIEDigitalLibrary.org/oe

Optimization of plasmonic cavity-resonant multijunction cells

Albert S. Lin
Sze-Ming Fu
Yan-Kai Zhong
Chi-Wei Tseng
Shih-yun Lai
Timothy Ching Kwok Lau



Optimization of plasmonic cavity-resonant multijunction cells

Albert S. Lin

Sze-Ming Fu

National Chiao-Tung University
Institute of Electronic Engineering
Hsinchu, Taiwan 30010
E-mail: hdt5746@gmail.com

Yan-Kai Zhong

National Chiao-Tung University
Department of Electro-Physics
Hsinchu, Taiwan 30010

Chi-Wei Tseng

Shih-yun Lai

Timothy Ching Kwok Lau

National Chiao-Tung University
Institute of Electronic Engineering
Hsinchu, Taiwan 30010

Abstract. Improving spectral photon harvesting is important for thin-film multijunction cells. We show that efficient spectral flux management can be achieved using genetic algorithm-optimized surface plasmon (SP) cavity-resonant type multijunction cells. We also observe that the excitation of the SP quasi-guided mode, Fabry–Perot mode, and SP polariton significantly enhance the photocurrent of multijunction cells. Two types of cavity structures are investigated. For the optimized SP intermediate reflector and bottom-grating cavity, the resonant cavity mode efficiently increases the long-wavelength absorption in the bottom cell by 63.27%, resulting in reduced absorbance asymmetry between the top and the bottom cells. Accordingly, the matched integrated absorbance is increased by 14.92%. For the optimized SP top- and bottom-grating (TBG) cavity, the integrated absorbance and current matching are improved due to the higher transmission through the solar cell front surface and the excitation of the quasi-guided mode with a more localized field in the bottom cell. The matched integrated absorbance is improved by 85.68% for the TBG cavity. © 2013 Society of Photo-Optical Instrumentation Engineers (SPIE) [DOI: 10.1117/1.OE.52.6.064002]

Subject terms: solar cell; surface plasmon; guided mode; multijunction cell.

Paper 121326 received Sep. 14, 2012; revised manuscript received May 18, 2013; accepted for publication May 28, 2013; published online Jun. 11, 2013.

1 Introduction

The use of multijunction cells, which are occasionally referred to as tandem cells, is a practical method to exceed the Schokley and Quessier limit of photovoltaic devices. Recently, surface plasmon (SP) photovoltaics have drawn considerable attention, because they can provide a new route to improve thin-film solar cell light-trapping below the diffraction limit.^{1–23} The SP phenomena that have been related to photovoltaics include localized surface plasmon,^{1,3,4,8,24} surface plasmon polariton (SPP),^{1,6,7,16,24} and far-field enhancement. Previous studies included a single metallic nanoparticle array on the top of a semiconductor layer^{1,3,16,25} to enhance photon forward scattering and plasmonic back reflectors showing SPP propagation along the metal/semiconductor interface.^{1,6,7,16,24} Although a single metallic grating on the top or on the bottom of the semiconductor thin-film effectively improved solar cell efficiency, cavity design is necessary to improve the efficiency even further. Here, the SP cavity design was applied to the multijunction cells. For multijunction cells, current matching is the most important consideration to maximize the efficiency; therefore, the subcells should have matched integrated absorbances. To optimize the geometrical parameters, a genetic algorithm (GA) was employed in this study. GA is a global search method that mimics natural evolution. It can identify a global maximum for ill-behaved objective functions, such as the optical cavity design, which is impossible to achieve using conventional optimization methods. The micromorphic silicon multijunction cell was used as an example to demonstrate the effectiveness of GA-optimized SP cavity for spectral flux management in the multijunction cells.

Micromorphic multijunction cells normally require a thick microcrystalline silicon ($\mu\text{-Si}$) bottom cell due to the low absorption coefficient of $\mu\text{-Si}$. Therefore, an SP microcavity can be employed to improve the absorbance of the $\mu\text{-Si}$ bottom cell and the current matching of the entire multijunction cell.

2 Surface Plasmon Structure and Calculation Procedure

In this study, the film thickness of the bottom $\mu\text{-Si}$ subcell was thinner than the value required to match the top amorphous silicon ($\alpha\text{-Si}$) cell. This situation better reflects the effect of the SP cavity on improving the bottom cell absorbance and the current matching. Figure 1 illustrates two types of cavity plasmonic design, which includes the intermediate reflector and bottom-grating (IRBG) cavity and the top- and bottom-grating (TBG) cavity.

Two types of cavity, i.e., plasmonic IRBG and plasmonic TBG are proposed. For the SP IRBG, the cavity consists of an Ag-back reflector, an Ag and ZnO bottom grating, a $\mu\text{-Si}$ thin film, Ag intermediate reflectors, and an $\alpha\text{-Si}$ thin film. For the SP TBG, the cavity consisted of an Ag back reflector, an Ag bottom grating, a $\mu\text{-Si}$ thin film, an $\alpha\text{-Si}$ thin film, and an Ag top grating. The optimization is performed by adjusting each geometrical parameter until the highest absorbance is obtained. The material parameters can be referenced in the literature.^{26–29} The silver parameter was obtained from Palik.³⁰ The silicon parameter was obtained from SOPRA. The ZnO parameter was obtained from the Hand Book of Optics, 2nd ed.³¹ The details of the integrated absorbance calculation can be obtained from Refs. 32–35. The Poynting vector and the absorption power density are

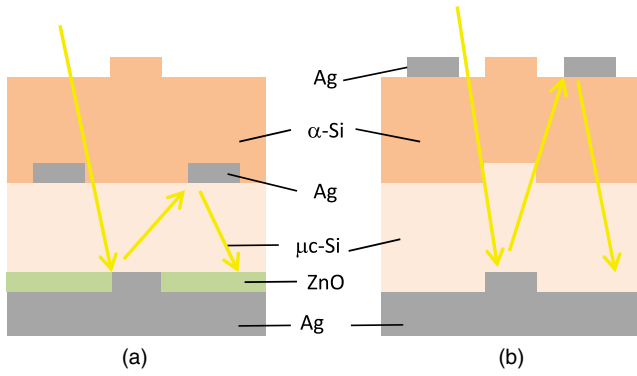


Fig. 1 Two designs of the surface plasmon (SP) cavity. (a) Intermediate reflector and bottom grating (IRBG) cavity, (b) and bottom-grating (TBG) cavity.

$$P_{\text{poynting}} = \vec{E}(\vec{r}) \times \vec{H}(\vec{r}) \quad P_{\text{absorption}} = \vec{E}(\vec{r}) \cdot \vec{J}(\vec{r}), \quad (1)$$

where the Poynting vector characterizes the incident power per unit area and the absorption power density characterizes the absorbed power per unit volume. The electromagnetic field is essentially a time-varying field, thus, a time-averaged quantity is of interest. The Poynting theorem under a harmonic steady state describes that the time-averaged inflow power equals the time-averaged absorbed power.

$$\begin{aligned} & \int_V P_{\text{absorption,avg}} dv + \int_S \vec{P}_{\text{poynting,avg}} \cdot d\vec{S} \\ &= \frac{1}{2} \int_V \text{Re}\{\vec{E}(\vec{r}) \cdot \sigma(\lambda) \vec{E}^*(\vec{r})\} dv \\ &+ \frac{1}{2} \int_S \text{Re}\{\vec{E}(\vec{r}) \times \vec{H}^*(\vec{r})\} \cdot d\vec{S} = 0, \end{aligned} \quad (2)$$

where σ is the conductivity of the materials. The absorbance is the absorbed power divided by the incident power.

$$A(\lambda) = \frac{\frac{1}{2} \int \text{Re}\{\sigma(\lambda) \vec{E}(\vec{r}) \cdot \vec{E}^*(\vec{r})\} d\vec{r}}{\frac{1}{2} \int \text{Re}\{\vec{E}(\vec{r}) \times \vec{H}^*(\vec{r})\} \cdot d\vec{S}}. \quad (3)$$

Next, the integrated absorbance is calculated by averaging $A(\lambda)$ weighted by the AM 1.5 solar spectrum.

$$\text{Int.Absorbance} = \frac{\int \frac{\lambda}{hc} S(\lambda) A(\lambda) d\lambda}{\int \frac{\lambda}{hc} S(\lambda) d\lambda}, \quad (4)$$

where $S(\lambda)$ is the AM 1.5 solar spectrum, h is the Planck constant, λ is the free space wavelength, and c is the speed of light. The photocurrent of each subcell can be directly determined by the integrated absorbance if the solar spectrum $S(\lambda)$ in Eq. (4) is in units of joule per unit time per unit area per unit wavelength ($\text{Js}^{-1}\text{cm}^{-2}\text{nm}^{-1}$).

In this work, the discretization of Maxwell's equation is performed using the two-dimensional (2-D) FEM using the COMSOL Multiphysics software package.³⁴ The incident light illumination on the solar cell is a transverse magnetic (TM)-polarized plane wave with wavelengths between 400 and 1000 nm, which is the wavelength range of interest for silicon materials. Only the TM-polarized wave is examined here, because a transverse electric (TE) wave does not

cause the surface plasmonic effect in 2-D.¹ Periodic boundary conditions are set at the left and right boundaries, whereas perfectly matched layer absorbing boundary conditions are used at the top and bottom boundaries of the computational domain. Next, the absorbance in silicon is calculated by integrating the divergence of the time-averaged Poynting vector. Only the absorbance in silicon generates an electron-hole, while the absorbance in metal causes SP absorption loss.

The optimization in this arrangement is only for TM-polarized light incident on one-dimensional grating structures in 2-D simulation domains. In 2-D problems, only TM wave excites the SP modes.⁴ For TE wave, the proposed geometry might not be optimal, and the absorbance for TE wave might not be boosted by the optimization procedure. Nonetheless, the optimization procedure in this study can be easily extended to three-dimensions. The 2-D simulation here illustrates the surface plasmonic enhancement associated with the TM-polarized light.^{1,3} In three-dimensional geometry, both TE and TM light will excite the SP modes. If the grating geometry is symmetric, e.g., circularly or squarely shaped gratings, the TE and TM responses are the same at normal incidence. In this case, the optimization can boost the absorbance of both polarizations, and can certainly boost the absorbance for unpolarized sunlight.

3 Optimization Procedures using Genetic Algorithm

A GA or an evolutionary algorithm is a stochastic global search method that mimics a natural biological evolution.³⁶ The principle of survival of the fittest is applied to a population of individuals, which are potential solutions to the problem. Individuals with higher fitness in the problem domain have a better chance to be selected and to reproduce their own offspring. This results in individuals who are better suited to the environment tending to have more children and higher fitness as the evolution process proceeds, just as in natural adaptation. GA is particularly suited for search in very large or unbounded sample spaces, and they have been proven useful in many different fields.³⁷⁻⁴⁰ For light coupling and trapping in solar cells, the complexity associated with the wave nature of light and the broad solar spectrum result in a similarly large sample space for the possible grating structures to optimize the solar cell absorbance. For a multijunction cell, the objective is to match the integrated absorbance for all of the subcells. This objective is referred to as current matching. Because the photocurrent of a multijunction cell is clamped by the subcell with the lowest integrated absorbance, the matched integrated absorbance is essentially the lowest integrated absorbance of all of the subcells.

$$\text{Lowest Int.Absorbance} \equiv \text{Matched Int.Absorbance}. \quad (5)$$

In this study, the terms "matched integrated absorbance" and "lowest integrated absorbance" of all of the subcells are used interchangeably for multijunction cells. The integrated absorbance is calculated by averaging the spectral absorbance weighted by the solar spectrum as indicated in Eq. (4). In this study, the lowest integrated absorbance of all subcells, *Lowest Int. Absorbance*, is defined as the objective function, and its value depends on the solar cell geometrical parameters:

$$\text{Lowest Int. Absorbance} = f(x_1, x_2, x_3, x_4, x_5, x_6, x_7), \quad (6)$$

where $x_1, x_2, x_3, x_4, x_5, x_6,$ and x_7 are the geometrical parameters, such as the grating depth, period, fill factor, etc. Only the absorbance in silicon contributes to the electron-hole pairs, and the metallic absorbance should be excluded. There are more specific definitions for the objective functions of the IRBG and TBG cavities, which will be provided later. For the objective functions with only one or two independent variables, an iteration over the entire search space can be used to locate the function maximum. Nonetheless, for functions with more variables, optimization is generally necessary. GA has been shown to be effective for locating the maxima of objective functions with a large number of independent variables.^{37,38}

4 Optimized Intermediate Reflector and Bottom Grating

Figure 2 illustrates the device structure of the IRBG cavity tandem cell. The structure is expected to significantly increase the bottom cell absorbance using SP photon interaction. FF_m is the fill factor of the intermediate reflector and FF_b is the fill factor of the bottom grating. The values $t_{g,m}$ and $t_{g,b}$ are the grating heights of the intermediate reflector and the bottom grating, respectively, ξ_m and ξ_b are the asymmetry factors of the intermediate reflector and the bottom grating, respectively, and Λ is the grating period. The objective function is defined as

$$\text{Lowest Int. Absorbance} = f(t_{g,m}, t_{g,b}, \xi_m, \xi_b, FF_m, FF_b, \Lambda). \quad (7)$$

For the micromorphic tandem cell, the bottom $\mu\text{-Si}$ absorption is always weaker than the top $\alpha\text{-Si}$ absorption, thus, the objective function is the integrated absorbance of the $\mu\text{-Si}$ cell. The optimization procedures were described in detail in Sec. 3. The optimized geometry is $FF_m = 0.1127$, $FF_b = 0.5825$, $t_{g,m} = 0.01 \mu\text{m}$, $t_{g,b} = 0.0743 \mu\text{m}$, $\xi_m = 0.3824 \mu\text{m}$, $\xi_b = 0.05 \mu\text{m}$, and $\Lambda = 0.5 \mu\text{m}$. In this study, the thicknesses of the $\alpha\text{-Si}$ and $\mu\text{-Si}$ layers were fixed at 60 and 400 nm, respectively.

Figure 3 shows the spectral responses for the top and the bottom subcells and their sum. The baseline cell was a planar

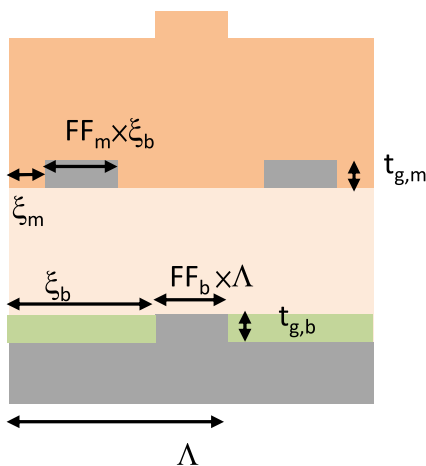


Fig. 2 Parameters to be optimized for the IRBG solar cell.

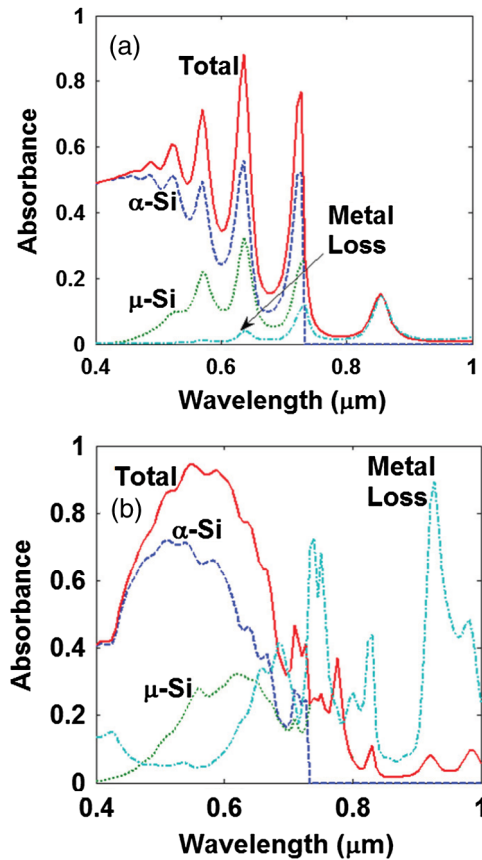


Fig. 3 (a) Baseline spectral response and (b) optimized IRBG cavity spectral response.

cell with a back reflector. The top cell is an $\alpha\text{-Si}$ cell, thus, its bandgap is larger than that of silicon, which was approximately $730 \mu\text{m}$. Hence, the spectral response of the $\alpha\text{-Si}$ top cell cuts off below $730 \mu\text{m}$, because the solar photon with wavelength longer than the $\alpha\text{-Si}$ bandgap did not contribute to the top cell photocurrent. The bottom cell is a $\mu\text{-Si}$ cell. This cell can absorb the photons with wavelengths above $730 \mu\text{m}$ that were not fully absorbed by the top cell, and can also absorb photons with wavelengths below $730 \mu\text{m}$. Figure 3 shows that the spectral response at long wavelengths is significantly improved by the SP IRBG structure. The quasi-guided mode excitation is significantly pronounced compared with the baseline, and a broad-band enhancement is achieved by the SP cavity. To quantify the broad-band enhancement, the integrated absorbance of wavelengths below $730 \mu\text{m}$ for the bottom cell is calculated as 0.0929, while that of the baseline cell was 0.0569. A 63.27% improvement in long-wavelength absorbance is achieved by the SP cavity due to the GA-optimized design and the SP photon interaction. The matched integrated absorbance, or equivalently the bottom cell integrated absorbance, for the full spectrum from 400 to 1000 nm is 0.1356 and 0.1180 for the optimized cavity and the baseline cell, respectively, and the improvement is 14.92%. The IRBG configuration is suitable when the material absorption of the bottom cell is weak, and light trapping is particularly important for long-wavelength photons. The enhancement of the bottom cell absorption for photons with wavelengths above $730 \mu\text{m}$ is not notably significant. Thus, in this

configuration, the top cell should be sufficiently thick to absorb all short-wavelength photons. Currently, notably few studies reported the metallic loss, and absorption cross-sections along the line of Mie scattering theory are commonly reported from the literature. Absorption in metal does not contribute to the electron-hole pairs and should be minimized. Fortunately, Fig. 3(a) and 3(b) shows that the metallic absorption is primarily at the long wavelength, where the silicon absorption is weak and the photons can arrive at the metal. These long-wavelength photons absorbed by the metal are unlikely to be absorbed by the silicon even in the absence of the metal, although the SP cavity enhances Si absorption at long wavelength. This result is evident given that the SP-cavity-type multijunction cell [Fig. 3(b)] has a much higher silicon absorbance than the baseline [Fig. 3(a)], although its metallic loss is also significantly higher than the baseline due to the SP excitation.

The quasi-guided mode excitation for the IRBG configuration was notably pronounced, which can be observed in the long-wavelength part of the spectral response. This result proves that through optimization, the cavity mode is excited, and the photon cavity lifetime is effectively extended.

Figure 4 shows the field profiles of the IRBG cavity structure. The unit in the color bar is not important because the Maxwell's equation is linear and the solution is scaled with the incident field. The absorbance is calculated by dividing the absorbed power in the silicon film by the incident power; the absolute value of the incident power and the field intensity do not affect the calculation result. For Fig. 4(a) and 4(b), the guided-mode excitation is of the Fabry-Perot type, where the pronounced layered profiles indicate that the photons bounce forth and back between the top and

the bottom facets. SPP is observed at the bottom grating where the silicon/silver and ZnO/silver dielectric-metal interfaces existed. The SPP exhibits a field intensity that was strongest at the interface, and decays away from the interfaces with the propagating constant $k_{x,SPP}$ along the interface. The SPP in-plane wave vector $k_{x,SPP}$ can be observed by a periodic field pattern along the interface direction, which is the x -direction here. In this work, the absorbance of the tandem cell is significantly increased using the properly optimized geometry, and the broad-band enhancement is achieved by the SP IRBG cavity design.

In Fig. 5(a) and 5(c), the field profiles of the scattering problem are shown where a total-field-scattered-field-like boundary condition is imposed on the air region. An incident solar wave propagates downward and impinges on the solar cell. Figure 5(b) and 5(d) plots the corresponding eigenmode profiles, where, unlike the scattering problem, no source is imposed on the top of the solar cell. The eigenmode excitation exists when the wave vector of the incident photons matches the wave vector of the Bloch mode at a specific frequency. The mode profile is essentially the field profile for the corresponding Bloch mode. The similarity between the field profiles for the scattering problem and the eigenmode problem is the direct evidence of quasi-guided mode excitations for the proposed optimal IRBG cavity. Generally, the total field can be factored into an incident field and a scattered field

$$H_T(\vec{r}) = H_{inc}(\vec{r}) + H_{scat}(\vec{r}) = H_0 \exp(ik_0y) + H_{scat}(\vec{r}), \quad (8)$$

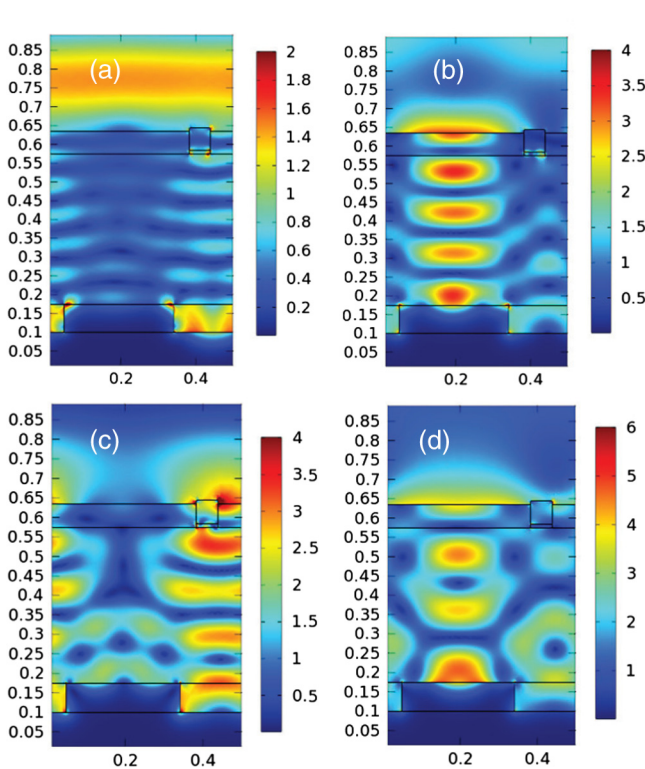


Fig. 4 Optimized cavity and field profiles at (a) $\lambda = 606.1$ nm, (b) $\lambda = 763.6$ nm, (c) $\lambda = 824.2$ nm, and (d) $\lambda = 921.2$ nm. The unit of length is μm .

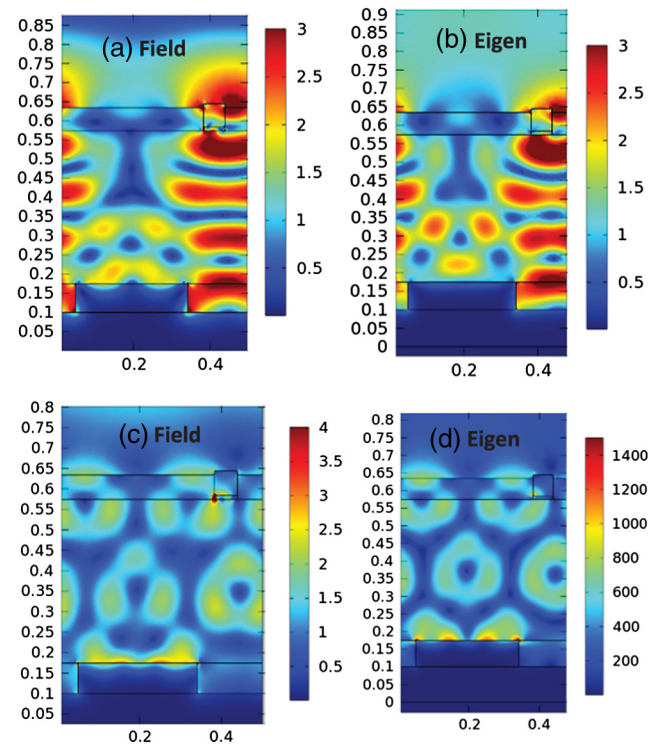


Fig. 5 (a) Field profiles for $\lambda = 0.8242 \mu\text{m}$, (b) corresponding eigenmodes for $\lambda = 0.8242 \mu\text{m}$, (c) field profiles for $\lambda = 0.8 \mu\text{m}$, and (d) corresponding eigenmodes for $\lambda = 0.8 \mu\text{m}$ for the optimized IRBG cavity. The unit of length is μm .

where H_0 is the incident magnetic field. Equation (8) assumes normal incidence and TM polarization, so that the wave propagates downward along the negative y -axis. To understand the similarity between the field profile and the eigenmode profile in Fig. 5, a simple transfer matrix method in standard electromagnetic theory is useful. Using simple backward matrix representation, the incident, scattered, and transmitted waves at a material interface can be expressed as

$$\begin{bmatrix} E_{\text{inc}} \\ E_{\text{scat}} \end{bmatrix} = \begin{bmatrix} b_{11} & b_{12} \\ b_{21} & b_{22} \end{bmatrix} \begin{bmatrix} E_{\text{trans}} \\ E_{\text{scat}2} \end{bmatrix}, \quad (9)$$

where b_{11} , b_{12} , b_{21} , and b_{22} are the matrix elements of the backward matrix. E_{inc} , E_{scat} , and E_{trans} are the incident, scattered, and transmitted waves, respectively, and $E_{\text{scat}2}$ is the scattered wave by the next material interface. Notice that E_{scat} , E_{trans} , and $E_{\text{scat}2}$ are the constituents of an eigenmode, but E_{inc} is not because there is no incident source field for the eigenmode problems. This point is easiest to understand by referring to the procedure of solving eigen-value problems using the transfer matrix method. If mode coupling is efficient, the majority of the incident power will be coupled into the corresponding eigenmode that consists of E_{scat} , E_{trans} , and $E_{\text{scat}2}$, and the corresponding eigen mode is excited. When the optical field confinement is strong inside the cavity, which is the requirement for light trapping, E_{inc} is diminished compared with E_{scat} , E_{trans} , and $E_{\text{scat}2}$ at the steady state. This fact and the efficient mode coupling result in the similar field profiles for the scattering and the eigenmode problems.

5 Optimized Top and Bottom Double Grating

Figure 6 illustrates the device structure for the TBG cavity tandem cell. We expected that the structure would significantly increase the absorption of both the top and the bottom cells using the SP photon interaction. FF_t is the fill factor of the top grating and FF_b is the fill factor of the bottom grating. The values $t_{g,t}$ and $t_{g,b}$ are the grating heights of the top and the bottom gratings, respectively, ξ_t and ξ_b are the asymmetry factors of the top and the bottom gratings, respectively, and Λ is the grating period. The objective function is defined as

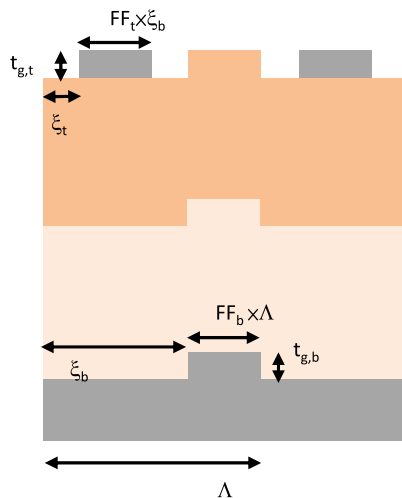


Fig. 6 Parameters to be optimized for the TBG cavity.

$$\text{Lowest Int. Absorbance} = f(t_{g,t}, t_{g,b}, \xi_t, \xi_b, FF_t, FF_b, \Lambda). \quad (10)$$

For a micromorphic tandem cell, the bottom $\mu\text{-Si}$ absorption is weaker than the top $\alpha\text{-Si}$ absorption. Thus, the objective function is the integrated absorbance in the $\mu\text{-Si}$ cell to make it approach the top $\alpha\text{-Si}$ cell integrated absorbance. The optimization procedure was described in detail in Sec. 3. The optimized geometry is $FF_t = 0.5$, $FF_b = 0.4746$, $t_{g,t} = 0.101 \mu\text{m}$, $t_{g,b} = 0.095 \mu\text{m}$, $\xi_t = 0.0495 \mu\text{m}$, $\xi_b = 0.2047 \mu\text{m}$, and $\Lambda = 0.4365 \mu\text{m}$. The thicknesses of the $\alpha\text{-Si}$ and $\mu\text{-Si}$ layers were fixed at 100 and 400 nm, respectively.

Figure 7 shows the spectral response of the plasmonic TBG cavity solar cell. The matched integrated absorbance for the full spectrum from 400 to 1000 nm is 0.1530 and 0.0824 for the optimized cavity and the baseline cell, respectively. The matched integrated absorbance is improved by 85.68% in reference to the baseline cell. The matched optical absorbance is what can actually contribute to the photocurrent in a series-connected multijunction cell. Because the photocurrent is clamped by the lower absorbance subcell in a series connection, the matched absorbance is the lowest absorbance of all of the subcells. The improvement of the TBG cavity is due to the transmission improvement at the multijunction cell front surface. Efficient spectral flux management is also an important factor in that, after the geometrical optimization, the excited-guided modes generally possess a higher field intensity at the bottom cell than at

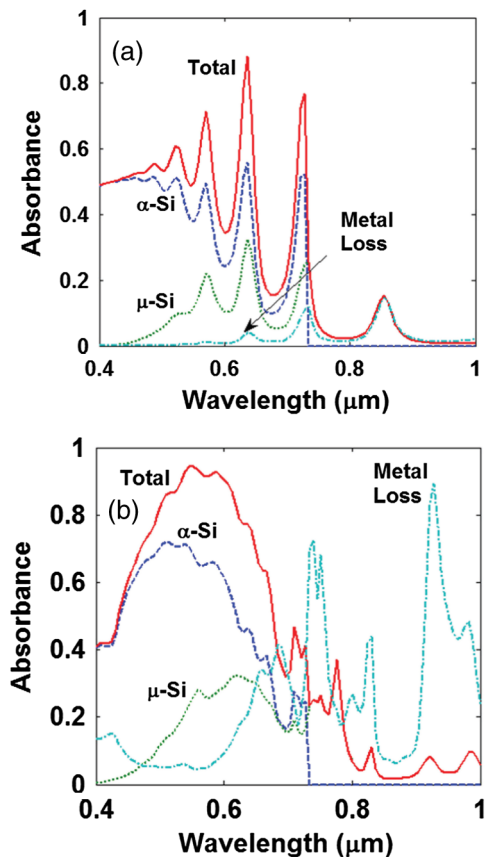


Fig. 7 (a) Baseline spectral response and (b) optimized TBG cavity spectral response.

the top cell, reducing the absorbance asymmetry between the subcells. The spectral flux management alleviates the insufficient absorbance and insufficient film thickness problems of the bottom $\mu\text{c-Si}$ cell. The metallic absorption losses for the baseline and the TBG cavity tandem cell are also shown in Fig. 7(a) and 7(b). Similar to the previous IRBG structure, the metallic losses are primarily at long wavelengths, where the silicon absorbance is weak. Although adding the SP grating structure increased the metallic absorption, the silicon absorbance is also significantly increased. This result reflects the importance of the optimization procedures, where the silicon absorbance is the physical quantity to be maximized. This study shows that the TBG-cavity-type configuration increased the matched absorbance using transmission improvement, light trapping and spectral-flux-balanced guided-mode excitation. The TBG cavity is particularly needed when the top cell subjects to insufficient absorption, i.e., ultra-thin SP solar cell, and when a significant portion of short-wavelength photons must be absorbed by the bottom cell. When a thicker top $\alpha\text{-Si}$ cell is used, the aforementioned IRBG structure is more suitable to boost the long-wavelength part of the absorbance. From the spectral response, the quasi-guided mode excitation for the TBG cavity is not significant because the top and the bottom Ag gratings are not as closely placed as for the IRBG structure. Therefore, the photons are likely to be absorbed before they could bounce back and forth between the top and the bottom gratings. The integrated absorbance of the optimized-TBG cavity cell is far above that of the baseline cell, indicating that the versatile design of the SP cavity is capable of identifying the most appropriate geometry for a specific purpose.

Figure 8 shows the field profiles for both the scattering and the eigenmode problems. The similarity between these field plots is also observed for the top and bottom grating cavities. This result indicates that the eigenmode excitation still exists for the top and bottom grating type structures, although in the spectral response [Fig. 7(b)], the absorption peak is not as pronounced as that in the IRBG cavity.

6 Detailed Balanced Limit for Multijunction Cells

For most studies on SP light trapping, only the optics aspect is considered. To obtain insight on the current matching improvement using the SP-cavity-type tandem cell, a detailed balance argument is employed below to show the real current voltage characteristics ($J - V$) of the tandem cells. The absorbed and emitted photon density can be expressed as⁴¹⁻⁴⁴

$$N(E_1, E_2, T, \mu) = \frac{2\pi}{h^3 c^2} \int_{E_1}^{E_2} \frac{1}{\exp\left(\frac{E-\mu}{kT}\right) - 1} E^2 dE, \quad (11)$$

where E_1 and E_2 are the integration limits, T is the temperature, and μ is the chemical potential, h is the Planck constant, c is the speed of light in a vacuum, and k is the Boltzmann constant. The current of the subcells can be written as⁴¹⁻⁴⁴

$$J_{\text{sub},i} = qN(E_{g,i}, \infty, T_{\text{SUN}}, 0) - qN(E_{g,i}, \infty, T_A, \mu_i), \quad (12)$$

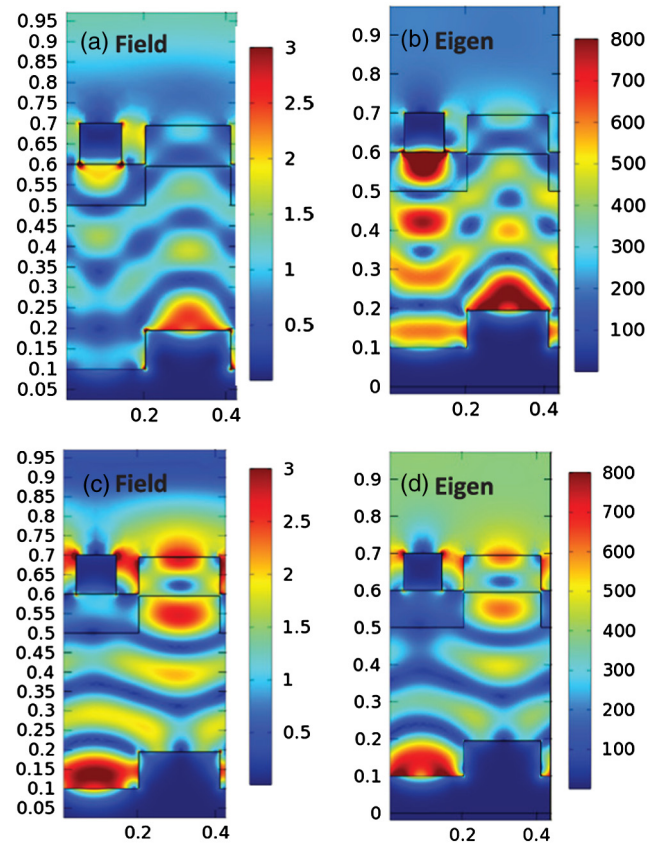


Fig. 8 (a) Field profiles for $\lambda = 0.9212 \mu\text{m}$, (b) corresponding eigenmode for $\lambda = 0.9212 \mu\text{m}$, (c) field profiles for $\lambda = 0.9879 \mu\text{m}$, and (d) the corresponding eigenmode for $\lambda = 0.9879 \mu\text{m}$ for the optimized TBG cavity. The unit of length is μm .

where $E_{g,i}$ is the bandgap of the semiconductor material for the i 'th subcell, T_{SUN} is the temperature of the sun, T_A is the ambient temperature, and μ_i is the chemical potential separation at subcell i . The expression in Eq. (12) is the ideal detailed balance argument where full absorption and emission are assumed. For more realistic devices, full absorption of solar photons is difficult to achieve and the light trapping determines the actual generated photocurrent, J_{ph} ,

$$J_{\text{ph}} = q \int \frac{\lambda}{hc} S(\lambda) A(\lambda) d\lambda. \quad (13)$$

The photocurrent of each subcell, $J_{\text{ph},i}$, is directly determined from the integrated absorbance for each subcell, which is evident by comparing Eqs. (4) and (13). The recombination current depends on the base-width W . The total current of the subcells for a more realistic device can therefore be written as

$$J_{\text{sub},i} = J_{\text{ph},i} - qN(E_{g,i}, \infty, T_A, \mu_i) A_f(W), \quad (14)$$

where A_f is the factor for the effect of the finite film thickness, which here was assumed to equal unity for the worst-case evaluation. To evaluate $J - V$, the constraints were necessary. The multijunction cell operation requires that the photocurrents of the subcells match each other, and the summation of the chemical potential separation of each subcell equals the applied voltage V_a :

$$J_{\text{sub},i} = J_{\text{sub},i+1}, \quad \sum_i \mu_i = V_a. \quad (15)$$

The detailed balance limit states that the selection of the bandgap is the primary consideration in achieving a balance between dark current and optical absorbance. For large bandgap materials, low dark current and low optical absorption are observed, while for small bandgap materials, high absorption and high dark current are observed. The multijunction cell is a practical method to exceed the Shockley–Queisser limit using different band-gaps for different energy ranges of solar photons. To achieve a high efficiency, current matching should be considered for the multijunction cell because the photocurrent is clamped by the subcell with the lowest photocurrent. For the IRBG structure, the photocurrent mismatch is reduced from 1.45 to 1.29, and for the TBG structure, the photocurrent mismatch is reduced from 2.61 to 1.91 using the GA optimization. Thus, the surface plasmonic cavity type tandem cell can significantly improve the current matching characteristics. Specifically for the micromorphic tandem cell, the higher temperature and thicker deposition of the bottom microcrystalline silicon cell are the sources of the elevated cost. Thus, the problem associated with the lower absorption coefficient of $\mu\text{-Si}$ can be overcome using the plasmonic effect if a proper design and optimization are achieved as illustrated in this work, which used GA.

In Fig. 9, the bottom cell absorbance is not fully matched to that of the top cell, especially for the TBG structure. As stated in Sec. 2, this result occurred because the $\mu\text{-Si}$ bottom cell thickness for all of the structures in this study is thinner than the value required to completely match the $\alpha\text{-Si}$ top cell absorbance. These thicknesses are chosen to better reflect the improvement of the bottom cell absorbance and the current matching by the SP cavity design. The thickness of the bottom cell can be easily increased or optimized, and a fully matched multijunction cell can be produced.

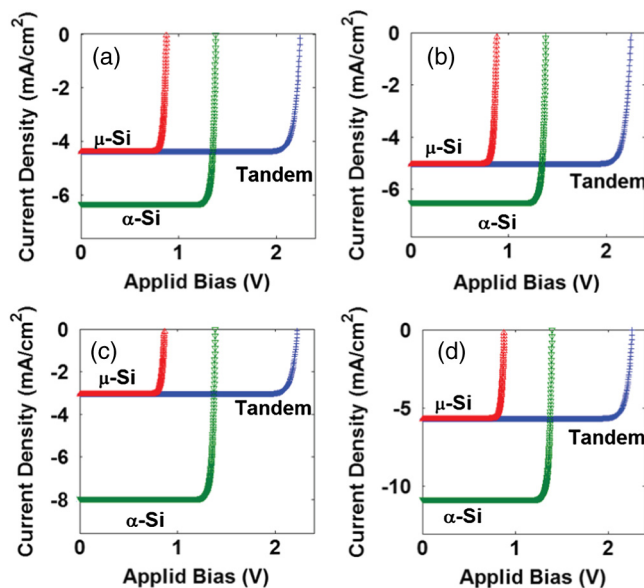


Fig. 9 Current-voltage for (a) the baseline of the IRBG cavity, (b) the optimized IRBG cavity, (c) the baseline of the TBG cavity, and (d) the optimized TBG cavity.

7 Conclusion

Here, two types of surface plasmonic cavity solar cells are optimized using GA. For the SP IRBG cavity, improved matched integrated absorbance is achieved by trapping the long-wavelength photons inside the bottom cavity through the quasi-guided mode excitations. For the SP TBG cavity, the matched absorbance is improved because the broad-band transmission was higher and the excitation of the quasi-guided mode has a more localized field in the bottom cell than in the top cell. Both surface plasmonic dual grating cavities show broad-band improvement in the absorbance and the improved spectral photon flux management, while the quasi-guided mode excitation is identified throughout the entire spectrum. This study demonstrated that using GA, the matched absorbance of SP multijunction cells can be effectively increased, facilitating tandem-cell current matching. This result also enables future design of a cavity-resonant-type solar cell with higher efficiency and reduced thickness.

Acknowledgments

We acknowledge the support of the high-speed computing facilities from the National Center of High-Performance Computing (NCHC), Hsinchu, Taiwan. The study was funded by the National Science Council (NSC), Taiwan.

References

1. K. Q. Le et al., "Comparing plasmonic and dielectric gratings for absorption enhancement in thin-film organic solar cells," *Opt. Express* **20**(S1), A39–A50 (2012).
2. Z. Yu and S. Fan, "Angular constraint on light-trapping absorption enhancement in solar cells," *Appl. Phys. Lett.* **98**(1), 011106 (2011).
3. M. Yang et al., "Incident angle dependence of absorption enhancement in plasmonic solar cells," *Opt. Express* **19**(s4), A763–A771 (2011).
4. W. E. I. Sha, W. C. H. Choy, and W. C. Chew, "Angular response of thin-film organic solar cells with periodic metal back nanostraps," *Opt. Lett.* **36**(4), 478–480 (2011).
5. U. W. Paetzold et al., "Design of nanostructured plasmonic back contacts for thin-film silicon solar cells," *Opt. Express* **19**(S6), A1219–A1230 (2011).
6. U. W. Paetzold et al., "Plasmonic reflection grating back contacts for microcrystalline silicon solar cells," *Appl. Phys. Lett.* **99**(18), 181105 (2011).
7. J. N. Munday and H. A. Atwater, "Large integrated absorption enhancement in plasmonic solar cells by combining metallic gratings and anti-reflection coatings," *Nano Lett.* **11**(6), 2195–2201 (2011).
8. N. Lagos, M. M. Sigalas, and E. Lidorikis, "Theory of plasmonic near-field enhanced absorption in solar cells," *Appl. Phys. Lett.* **99**(6), 063304 (2011).
9. F.-J. Haug et al., "Resonances and absorption enhancement in thin film silicon solar cells with periodic interface texture," *J. Appl. Phys.* **109**(8), 084516 (2011).
10. F. J. Beck, S. Mookkapatil, and K. R. Catchpole, "Light trapping with plasmonic particles: beyond the dipole model," *Opt. Express* **19**(25), 25230–25241 (2011).
11. S. Zanotto, M. Liscidini, and L. C. Andreani, "Light trapping regimes in thin-film silicon solar cells with a photonic pattern," *Opt. Express* **18**(5), 4260–4274 (2010).
12. K. Söderström et al., "Photocurrent increase in n-i-p thin film silicon solar cells by guided mode excitation via grating coupler," *Appl. Phys. Lett.* **96**(21), 213508 (2010).
13. C. Min et al., "Enhancement of optical absorption in thin-film organic solar cells through the excitation of plasmonic modes in metallic gratings," *Appl. Phys. Lett.* **96**(13), 133302 (2010).
14. S. B. Mallick, M. Agrawal, and P. Peumans, "Optimal light trapping in ultra-thin photonic crystal crystalline silicon solar cells," *Opt. Express* **18**(6), 5691–5706 (2010).
15. F. J. Beck, S. M. Polman, and K. R. Catchpole, "Asymmetry in photocurrent enhancement by plasmonic nanoparticle arrays located on the front or on the rear of solar cells," *Appl. Phys. Lett.* **96**(3), 033113 (2010).
16. H. A. Atwater and A. Polman, "Plasmonics for improved photovoltaic devices," *Nat. Mater.* **9**, 205–213 (2010).
17. P. N. Saeta et al., "How much can guided modes enhance absorption in thin solar cells," *Opt. Express* **17**(23), 20975–20990 (2009).

18. A. Meyer and H. Adea, "The effect of angle of incidence on the optical field distribution within thin film organic solar cells," *J. Appl. Phys.* **106**, 113101 (2009).
19. W. Bai et al., "Design of plasmonic back structures for efficiency enhancement of thin-film amorphous Si solar cells," *Opt. Lett.* **34**(23), 3725–3727 (2009).
20. D. Cheyng et al., "The angular response of ultrathin film organic solar cells," *Appl. Phys. Lett.* **92**(24), 243310 (2008).
21. K. R. Catchpole and A. Polman, "Plasmonic solar cells," *Opt. Express* **16**(26), 21793–21800 (2008).
22. V. E. Ferry et al., "Light trapping in ultrathin plasmonic solar cells," *Opt. Express* **18**(S2), A237–A245 (2010).
23. A. Lin et al., "An optimized surface plasmon photovoltaic structure using energy transfer between discrete nano-particles," *Opt. Express* **21**(S1), A131–A145 (2013).
24. H.-Y. Lin et al., "Surface plasmon effects in the absorption enhancements of amorphous silicon solar cells with periodical metal nanowall and nanopillar structures," *Opt. Express* **20**(S1), A104–A118 (2012).
25. S. Pillai et al., "The effect of dielectric spacer thickness on surface plasmon enhanced solar cells for front and rear side depositions," *J. Appl. Phys.* **109**(7), 073105 (2011).
26. J. M. Khoshman and M. E. Kordesch, "Optical constants and band edge of amorphous zinc oxide thin films," *Thin Solid Films* **515**, 7393–7399 (2007).
27. S. J. Kang and Y. H. Joung, "Influence of substrate temperature on the optical and piezoelectric properties of ZnO thin films deposited by RF magnetron sputtering," *Appl. Surf. Sci.* **253**(17), 7330–7335 (2007).
28. C. Munuera et al., "Morphology of ZnO grown by MOCVD on sapphire substrates," *J. Cryst. Growth* **264**(1–3), 70–78 (2004).
29. A. S. Ferlauto et al., "Analytical model for the optical functions of amorphous semiconductors and its applications for thin film solar cells," *Thin Solid Films* **455–456**, 388–392 (2004).
30. E. D. Palik, *Handbook of Optical Constants of Solids*, Academic Press Handbook Series, Academic Press, San Diego, CA (1985).
31. Optical Society of America, *Handbook of Optics, Vol. 2: Devices, Measurements, and Properties*, M. Bass, Ed., 2nd ed., McGraw-Hill Professional, New York (1994).
32. A. Lin and J. D. Phillips, "Optimization of random diffraction gratings in thin-film solar cells using genetic algorithms," *Sol. Energ. Mat. Sol.* **92**(12), 1689–1696 (2008).
33. P. Bhattacharya, *Semiconductor Optoelectronic Devices*, 2nd ed., Prentice-Hall, Upper Saddle River, NJ (2006).
34. Comsol AB, *Comsol Multiphysics RF Module User Guide V 3.3*, Burlington, MA (2006).
35. Synopsys, "Sentaurus device EMW user manual V. X-2005.10," pp. 78–79, Mountain View, CA (2005).
36. A. Chipperfield et al., *Genetic Algorithm Toolbox User Guide*, University of Sheffield, Sheffield, UK (1994).
37. S. Preblea, M. Lipson, and H. Lipson, "Two-dimensional photonic crystals designed by evolutionary algorithms," *Appl. Phys. Lett.* **86**(6), 061111 (2005).
38. B. Deken, S. Pekarek, and F. Dogan, "Minimization of field enhancement in multilayer capacitors," *Comput. Mater. Sci.* **37**(3), 401–409 (2006).
39. H. Lipson and J. B. Pollack, "Automatic design and manufacture of robotic lifeforms," *Nature* **406**, 974–977 (2000).
40. L. Shen, Z. Ye, and S. He, "Design of two-dimensional photonic crystals with large absolute band gaps using a genetic algorithm," *Phys. Rev. B* **68**(3), 035109 (2003).
41. G. Wei et al., "Thermodynamic limits of quantum photovoltaic cell efficiency," *Appl. Phys. Lett.* **91**(22), 223507 (2007).
42. A. S. Brown and M. A. Green, "Impurity photovoltaic effect: fundamental energy conversion efficiency limit," *J. Appl. Phys.* **92**(3), 1329–1336 (2002).
43. A. Luque and A. Martí, "Increasing the efficiency of ideal solar cells by photon induced transitions at intermediate levels," *Phys. Rev. Lett.* **78**(26), 5014–5017 (1997).
44. M. J. Keevers and M. A. Green, "Efficiency improvements of silicon solar cells by the impurity photovoltaic effect," *J. Appl. Phys.* **75**(8), 4022–4031 (1994).

Biographies and photographs of the authors not available.